Journal of Rock Mechanics and Geotechnical Engineering 17 (2025) 1862–1875

Contents lists available at ScienceDirect

Journal of Rock Mechanics and Geotechnical Engineering

journal homepage: www.jrmge.cn

Full Length Article

A unique time-dependent deformation behavior of coral reef limestone

Kai Wu [a, b], Qingshan Meng [a, b, *], Le Luo [a, b], Qinglong Qin [c], Chi Wang [a, b], Xinzhi Wang [a, b], Tianli Shen [a, b], Haozhen Ding [a, b]

[a] State Key Laboratory of Geomechanics and Geotechnical Engineering, Institute of Rock and Soil Mechanics, Chinese Academy of Sciences, Wuhan, 430071, China
[b] University of Chinese Academy of Sciences, Beijing, 100049, China
[c] Department of Civil and Environmental Engineering & Research Centre for Resources Engineering Towards Carbon Neutrality, The Hong Kong Polytechnic University, Hong Kong, 999077, China

ARTICLE INFO

Article history:
Received 15 December 2023
Received in revised form
28 March 2024
Accepted 14 May 2024
Available online 24 May 2024

Keywords:
Coral reef limestone
Time-dependent deformation
Creep mechanism
Constitutive model

ABSTRACT

Catastrophic failure in engineering structures of island reefs would occur when the tertiary creep initiates in coral reef limestone with a transition from short-to long-term load. Due to the complexity of biological structures, the underlying micro-behaviors involving time-dependent deformation are poorly understood. For this, an abnormal phenomenon was observed where the axial and lateral creep deformations were mutually independent by a series of triaxial tests under constant stress and strain rate conditions. The significantly large lateral creep deformation implies that the creep process cannot be described in continuum mechanics regime. Herein, it is hypothesized that sliding mechanism of crystal cleavages dominates the lateral creep deformation in coral reef limestone. Then, approaches of polarizing microscope (PM) and scanning electronic microscope (SEM) are utilized to validate the hypothesis. It shows that the sliding behavior of crystal cleavages combats with conventional creep micro-mechanisms at certain condition. The former is sensitive to time and strain rate, and is merely activated in the creep regime.

1. Introduction

Dead coral polyps undergo diagenesis to form coral reef limestone (CRL). Different coral species and diagenetic environments bring complex pore structures to coral reef limestone, making them mechanically anisotropic (Zheng et al., 2020). CRL contains more than 90% $CaCO_3$, and the main mineral composition of calcified corals that are not subjected to intact diagenesis is aragonite or high-magnesium calcite, whereas the main mineral of CRL is low-magnesium calcite (Meng et al., 2022). Although the mineral composition of CRL is similar to that of terrestrial limestone (Brantut et al., 2014a; Nicolas et al., 2017), the heterogenous degree of terrestrial limestones is significantly smaller than that of CRL. The deformation and evolutionary law of CRL over time concerns the stability of the island reefs and the shallow coral ecosystems (Guppy, 1882, 1889; Gove et al., 2023).

The time-dependent behaviors of rock under constant stress are generally attributed to the sub-critical crack growth, namely the stress corrosion effect (Brantut et al., 2012; Cong and Hu, 2017). Creep is usually divided into instantaneous creep (primary creep), steady creep (secondary creep), and accelerated creep (tertiary creep) according to the strain rate (Zhao et al., 2019). The creep damage of rock depends on duration, and the damage degree and mechanism are varied in different creep stages (Cheng et al., 2021). In addition, the creep behaviors of rocks under constant stress depend on many factors, such as confining pressure, deviatoric stress, water content, temperature, and stress level (Weidinger et al., 1997; Yang et al., 1999; Roberts et al., 2015). Saturated rocks with low-to-medium strength usually exhibit significant creep behavior under a high-stress ratio (Brantut et al., 2014a; Yang et al., 2014). CRL has remained saturated over a long period of time due to

* Corresponding author. State Key Laboratory of Geomechanics and Geotechnical Engineering, Institute of Rock and Soil Mechanics, Chinese Academy of Sciences, Wuhan, 430071, China.
E-mail address: qsmeng@whrsm.ac.cn (Q. Meng).
Peer review under responsibility of Institute of Rock and Soil Mechanics, Chinese Academy of Sciences.

https://doi.org/10.1016/j.jrmge.2024.05.006

its marine diagenetic environment and well-developed pore network, and its strength ranges from exceedingly soft rock to relatively hard rock with four types (GB/T 50218-2014, 2015; Wu et al., 2022b). Over elapsed time, the islands and reefs will experience rheology under long-term tectonic stress and geo-stress.

Water can reduce the surface energy of calcite, thereby promote the subcritical crack growth and pressure dissolution (Zhang et al., 2010; Liteanu et al., 2013). Creep damage in limestone undergoes a brittle-ductile transition at room temperature with increasing confining pressure (Heard, 1960; Evans et al., 1990; Wong and Baud, 2012), which depends on several parameters such as porosity, pore size, and particle size. Limestone creep results from the coupling of microcrack, intragranular plastic deformation, and water-induced effects (e.g. subcritical crack growth and pressure dissolution). At the microscale, there are potential competing mechanisms among subcritical crack growth, intragranular plastic rheology, and pressure dissolution (Brantut et al., 2014a). Moreover, the strain rate of rocks is sensitive to the stress level applied, and the creep deformation requires less energy than deformation under quasi-static compression (Brantut et al., 2014a; Nicolas et al., 2017). Even though the creep characteristics of stress are well understood, however, a large amount of biopores and bioclasts in CRL, together with the above-mentioned microscopic mechanisms, will control the creep characteristics of CRL. Currently, research on CRL mainly involves the strength properties and damage mechanisms under quasi-static loads (Zhang et al., 2022b), dynamic responses under impact loads (Meng et al., 2024), pile-rock interactions (Zhang et al., 2022a), surrounding rock stability evaluation (Tang et al., 2018), and shallow stratum stability assessment (Wu et al., 2022). Unfortunately, there is still a research gap in the rheological mechanisms of CRL in the creep regime, for the long-term stability assessment of island reef infrastructure. For this, this study conducted quasi-static triaxial tests and stress-stepping creep tests on the CRL to analyze the mechanical behaviors of the CRL under constant strain rate and stress level as well as to gain insights for the underlying micromechanism of its time-dependent deformation behaviors. Finally, a constitutive model describing the unique creep characteristics of CRL was proposed.

2. Methods

2.1. Specimen preparation

Soft and hard interbedded structures characterize the CRL strata of the islands (Wu et al., 2023b), and the wave energy and depth create different depositional environments, resulting in noticeable structural differences in CRL (Wu et al., 2022a, 2023a). According to the structure-component principle, the CRL is classified as coral framework limestone (CFL), coral boulder limestone (CBL), coral gravel limestone (CGL), and coral calcarenite limestone (CCL) (Zhao et al., 1992). The CFL and CBL cores were drilled from a reef island in the South China Sea with ranges of 75–79 m and 138–140 m, respectively. The sampling depths are in the regium where the underground engineering is sited. The test specimens belonged to CFL and CBL, which were densely cemented with low porosity. The CBL had large dissolution pores and coral growth lines inside. Table 1 displays the physicomechanical parameters of the specimens, among which the dry density and *P*-wave velocity of CFL were significantly higher than those of CBL. Creep tests were conducted using a stress-control scheme, and the strength prediction method based on the pore fractal dimension was adopted to predict the strength of the four types of reef limestone specimens before the tests (Wu et al., 2022b). The CFL and CBL specimens were distributed with dissolution pores and microbial holes on their surfaces.

Eight specimens were prepared for each of the two specimen types, four of which were the specimens for uniaxial and triaxial creep tests. Fig. 1 visualizes the pore structure distribution of CFL and CBL. Box-counting method was extensively utilized to characterize the complexity and heterogeneity of the object (Huang et al., 2014). The box counting-based fractal dimensions of pore structure of CFL and CBL depicted in Fig. 1 are 2.092 and 2.481, respectively, indicating that the pore structure of CFL is more heterogenous than that of CBL. The specimens were cylindrical with a diameter of 50 mm and a height of 100 mm to fulfill the requirement of a 2:1 height-to-diameter ratio specified by ISRM (Ulusay, 2015). The specimens were sealed with thermoplastic tubes prior to testing, and the confining pressure was applied by compressing the thermoplastic tubes with hydraulic fluid. To avoid the hydraulic oil filling to pier powder still that was difficult to fill with cement powder, the rubber cement was used to fill the end defects when the specimens were packaged (Fig. 1).

2.2. Experimental procedure

The triaxial tests (i.e. quasi-static condition) at constant strain rate were performed by MTS815.04 rock testing system, and the stress-stepping creep tests at constant stress were performed by RC-2000 rock servo triaxial rheology tester. The confining pressures were set to 0 MPa, 1 MPa, 2 MPa, and 4 MPa, respectively, and the computed tomography (CT) scans were performed to obtain the pore information of CRL specimens before the tests for the purpose of predicting the peak strength σ_p at the corresponding pressures, with a spatial resolution of 56 μm. Avizo platform was utilized to visualize and analyze the CT scanning data. Subsequently, the CRL specimens were saturated with vacuum to simulate the seawater-saturated environment. The triaxial test at quasi-static condition was loaded at a strain rate order of 10^{-5} s^{-1}, with a data acquisition frequency of 5 Hz and an accuracy of 10^{-6}. For the creep test at constant stress scenario (i.e. creep condition), σ_p was divided into ten stages. The specimen was first preloaded by applying an axial force of 1 kN, and then was hydrostatically pressurized to the target value. The first level of loading was 40% of σ_p, and then the pressure was kept constant. The next level of loading was carried out when the deformation was less than 1 μm for 24 h until the specimen underwent accelerated creep and finally failed (see Fig. 1). The loading rate was 100 N/s, and the data acquisition frequency was set to be once every 0.05 min during 0–2 h, once every 10 min during 2–5 h, and once every 30 min after 5 h of creep. As the rheological characteristics of rock materials are sensitive to temperature, the room temperature remains constant at 25 °C during testing period. After the creep test was completed, the specimen was placed in a gel to maintain its destructive form to facilitate production of the petrographic thin section, which were sampled perpendicular to the maximum principal stress σ_1 (see red markers in Fig. 1). Finally, the cracked rock slices were observed under a polarizing microscope to investigate the interaction between the crystal particles and the microcracks during the creep process.

2.3. Strain rate calculation

The test adopted a stress-stepping creep loading method, where the loading deformation under constant strain rate and the creep deformation under constant stress in each loading step were differentiated according to the stress change. The axial deformation of the specimen was the average of the two linear variable differential transformer (LVDT) signals, which effectively corrected the error caused by specimen distortion. The lateral deformation was measured by chain LVDT. The data acquisition time step during the creep test changed over elapsed time, and the sensor noise was

Table 1
The physical parameters of coral reef limestone.

Specimen	Confining pressure (MPa)	Dry density (g/cm^3)	*P*-wave velocity (m/s)	Porosity (%)	Predicted UCS (MPa)
CFL	0	2.63	4445.38	4.52	32.08
	1	2.66	4597.46	4.64	57.88
	2	2.64	4526.37	4.55	71.37
	4	2.60	4293.3	4.40	127.17
CBL	0	2.47	3881.81	8.47	15.34
	1	2.45	3803.39	8.31	18.45
	2	2.44	3764.28	8.17	34.08
	4	2.46	3845.26	8.35	54.05

Note: UCS is the uniaxial compression strength.

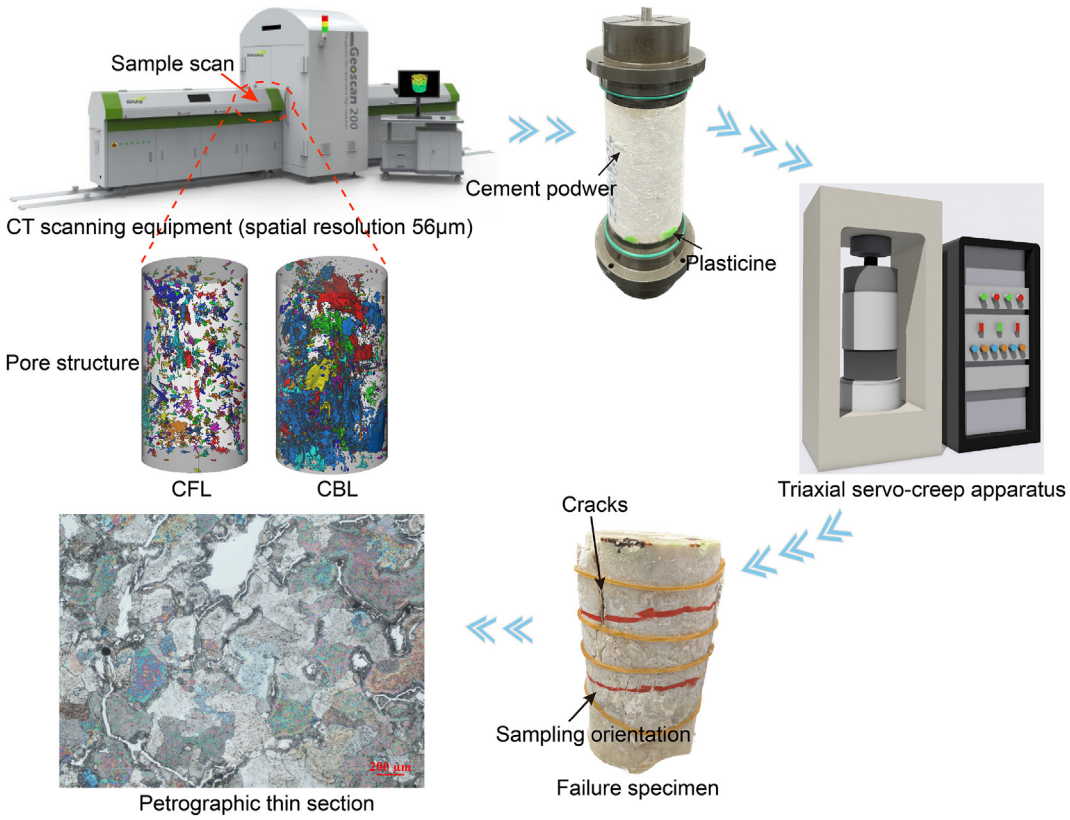

Fig. 1. Schematical diagram of the experimental procedure.

amplified when the creep strain rate was calculated for each loading stage from discrete data at fixed intervals. Therefore, in the strain rate calculation, de-noising was performed by Chebyshev interpolation (Effenberger and Kressner, 2012). For island deformation, it is crucial to determine the time to reach steady creep and the rate of steady creep. Therefore, this paper calculated the steady creep rate $\dot{\varepsilon}_S$ in creep deformation based on the polyfit $(\cdot)$ function in the NumPy package of Python, and obtained the onset of steady creep by $|\dot{\varepsilon} - \dot{\varepsilon}_S| \leq \xi$, where $\dot{\varepsilon}$ is the strain rate during the creep phase, and ξ is a positive number as small as possible that needs to be adjusted in the calculation according to the characteristics of the data set.

3. Results

3.1. Stress-strain relationship under constant strain rate

To explore the time-dependent deformation characteristics of CRL, two types of structural CRLs underwent compression tests under constant strain rate (in the order of 10^{-5}) and constant stress. The results in Fig. 2 indicate that both types of CRLs underwent the same deformation stage until ultimate brittle failure occurred. As the deviatoric stress increased, the specimens experienced four typical stages before failure. These included the compaction stage (*OA*) and linear elastic deformation stage (*AB*), in which the crack volume inside the specimens was constant, and the crystal experienced elastic compression. Subsequently, cracks in specimens initiated at the onset of the *BC* stage, and the specimen pores were further compacted (see Fig. 2). The inelastic compaction in the stable crack propagation stage was an instantaneous phenomenon (Baud et al., 2000). With increasing deviatoric stress, the volumetric strain yielded shearing dilatancy after the critical inflection point *C* (Fig. 2), indicating that the volumetric deformations of specimens were dominated by crack nucleation and propagation. Therefore, in the *CD* stage, cracks began to propagate unstably, and shear fracture became localized. The specimens suffered brittle failure at point *D*

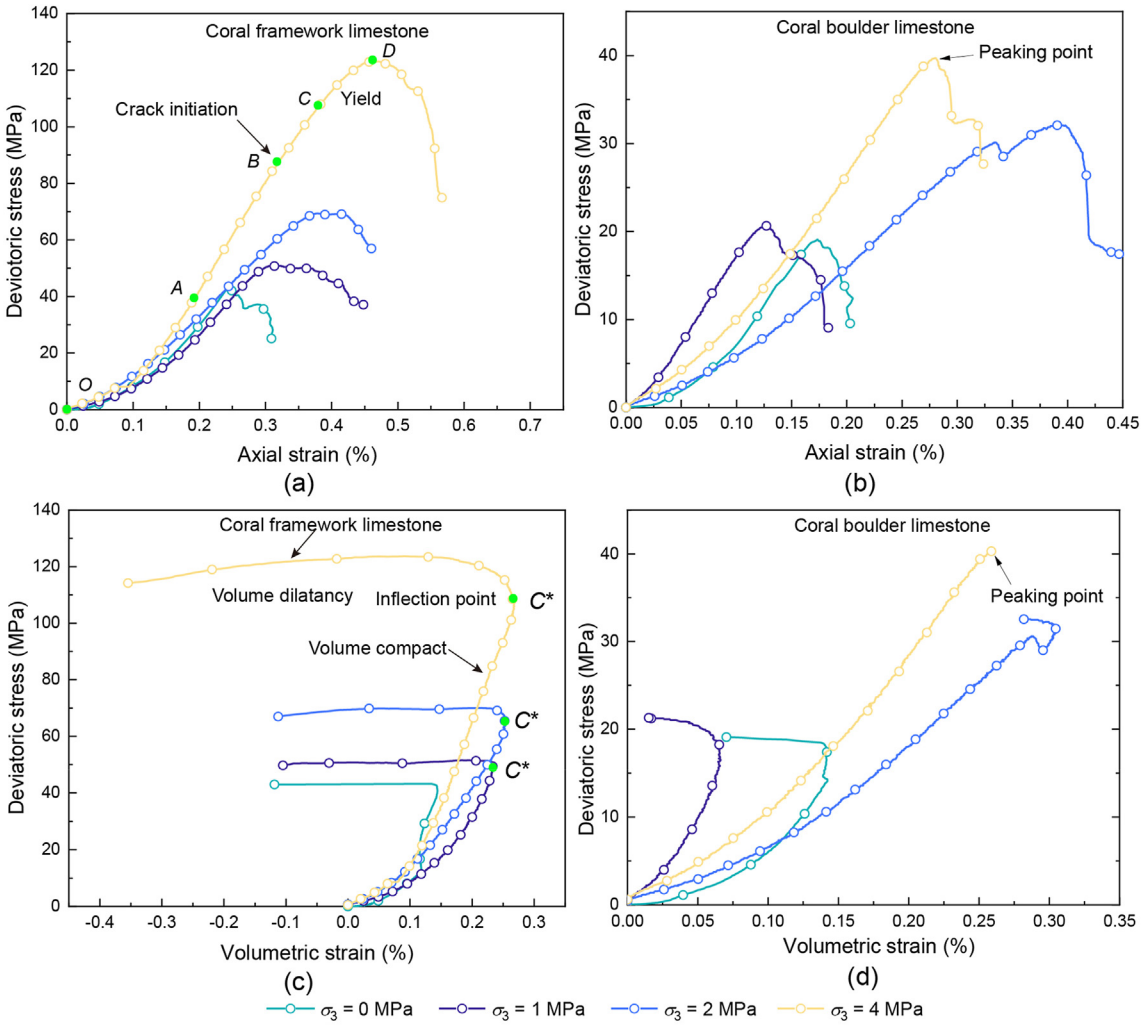

Fig. 2. Stress-strain curves of CFL and CBL: (a) and (b) are curves with respect to deviatoric stress versus axial strain, (c) and (d) are curves with respect to deviatoric stress vs. volumetric strain.

with a sudden stress drop, and local cracks penetrated to form a shear rupture surface.

Table 2 summarizes the strengths and peak strains of CRL with two structures under different confining pressures. The constraint effect of confining pressure significantly increased the strengths of the specimens. Tavel limestone are 14.7% in porosity and 242.7 MPa and 292.3 MPa in strengths at confining pressures of 55 MPa and 70 MPa (measuring methods of porosity and strengths were described in detail by Nicolas et al. (2017)), respectively. Nicolas et al. (2017) reported that the strength is negatively related to porosity, however, the previous work (Wu et al., 2023a) supported that the mechanical strength of the specimen was not only affected by porosity but also by pore size and pore complexity after analyzing the core database of CRL. The two types of CRL specimens in Fig. 2a and c experienced short-term strain hardening at a constant strain rate (i.e. 10^{-5} s^{-1}). Subsequently, the stress reached the peak after the specimens experienced a short-term strain hardening, followed by a significant stress drop, representing apparent brittle failure. Therefore, when the confining pressure did not exceed 4 MPa, the deformations of CFL and CBL were typical of brittle regime.

Table 2
The deformation and strength parameters of CRLs subjected to constant strain rate.

CRL	Confining pressure (MPa)	Peaking strength (MPa)	Peaking strain (%)
CFL	0	43.24	0.24
	1	50.88	0.32
	2	69.25	0.38
	4	123.09	0.47
CBL	0	19.10	0.17
	1	20.71	0.13
	2	32.08	0.40
	4	39.72	0.28

3.2. Brittle creep

The porosity of the two types of CRL specimens used in the creep tests is similar to that observed in the constant strain rate tests and falls within the range shown in Table 1. The two types of specimens encountered macroscopic failure after experiencing multi-step creep. Four CFL specimens underwent accelerated creep and failed under the last stress step (with deviatoric stresses of 97.35 MPa, 117.27 MPa, 140.76 MPa, and 170.06 MPa for confining pressure of 0 MPa, 1 MPa, 2 MPa, and 4 MPa, respectively), while three CBL specimens failed suddenly during quasi-static loading (Fig. 3a and b). The peak strength of the two types of CRL increased

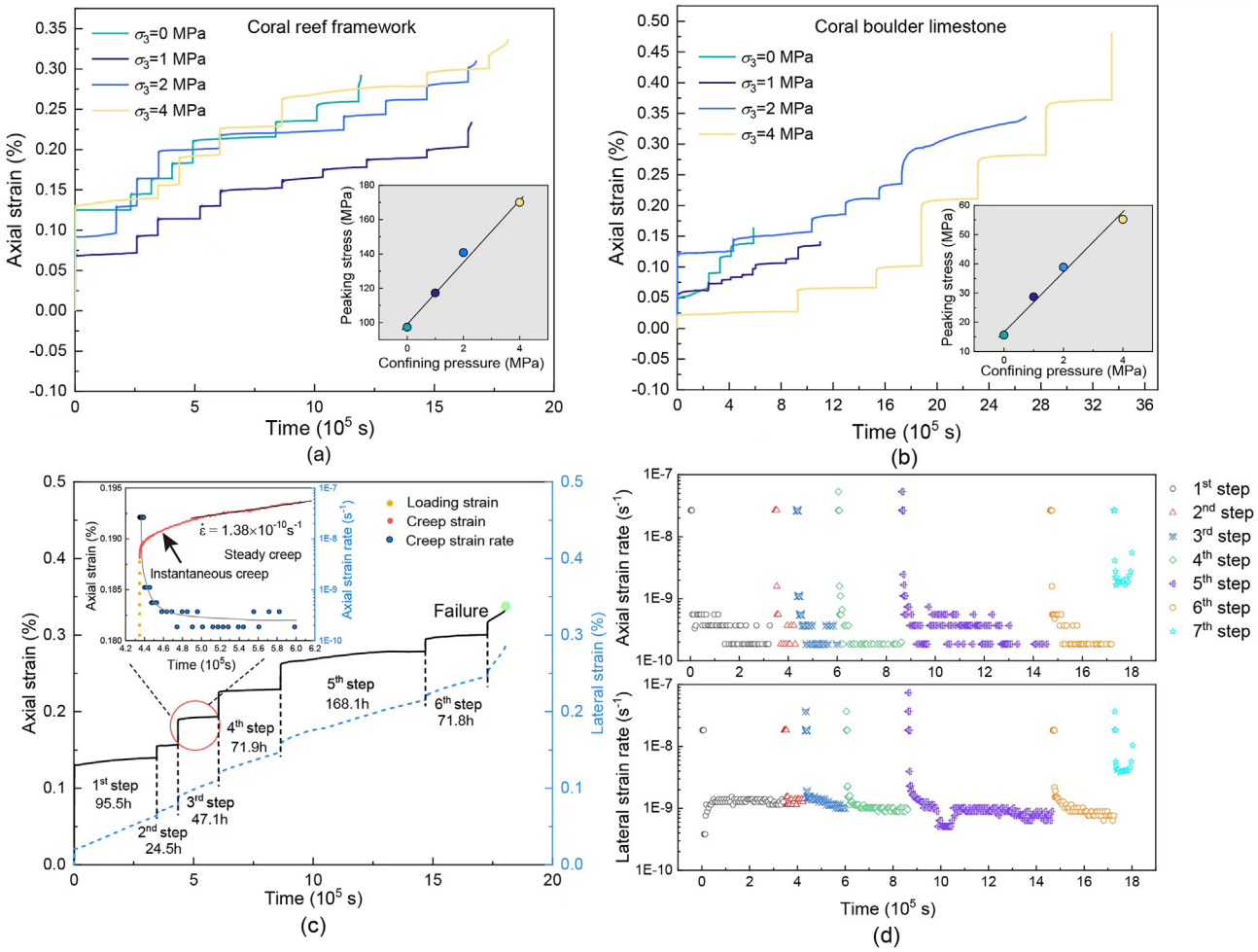

Fig. 3. Deformation evolution of CRL under different confining pressures: (a) and (b) are the curves with respect to the axial strain versus time of CFL and CBL subjected to stepping-stress, (c) is the comparison between axial strain and lateral strain with respect to time (including the loading stage with constant strain rate and the creep stage with the constant stress), and (d) axial and lateral strain rates versus time.

linearly with increasing confining pressure under the stepping load, and the peak strength of the CFL was significantly higher than that of the CBL. Furthermore, the creep time of specimens increased with confining pressure. However, there was no apparent tendency in the final peak strain, which was attributed to the natural variability in between the specimens.

Fig. 3c shows the lateral strain and axial strain of a typical specimen for analysis. The constant stress was maintained after completing the quasi-static loading. The specimen underwent the instantaneous creep stage, followed by a steady deformation at a constant rate of 1.38×10^{-10} s^{-1} (steady creep). At the last stress step, the specimen encountered an accelerated creep stage and failed. Note that the lateral creep strain of CRL at each stress step was significantly greater than the axial creep strain, and the lateral creep rate was also significantly greater than the axial creep rate (see Fig. 3d), which was different to that of traditional rocks, such as sandstone, granite, and mudstone (Maranini and Yamaguchi, 2001; Yang et al., 2014; Wang et al., 2021; Xue et al., 2022; Fang et al., 2023). In addition, a similar phenomenon was also noticed in diabase, and the specimen underwent volume dilatancy in the initial creep stage, but no relevant explanation was provided (Zhang et al., 2011). In this study, the Poisson's ratios (defined as the ratio of lateral strain to axial strain) during the creep of the CRL were all greater than 1, but the Poisson's ratios during quasi-static loading returned to normal, which revealed that the Poisson's ratio did not constrain the lateral and axial creep deformations of CRL.

3.3. Strain rate

The specimen initially underwent elastic compaction until the stress was increased to the critical transition pressure C^* that converts volume compaction to volume dilatancy. After exceeding C^*, the specimen underwent volume dilatancy, which was typical of the brittle regime. The minimum strain rate of the specimen (i.e. the steady creep stage) was generally considered to reflect the sensitivity of strain rate to stress. The minimum strain rate of rock usually undergoes a process of initial decrease followed by an increase. It has been recognized that the specimen will not encounter accelerated creep when the deviatoric stress Q is less than a critical value, and the axial deformation will converge. Therefore, this paper took CFL as an example to investigate the sensitivity of the minimum strain rate $\dot{\varepsilon}_{\min}$ to stress in the volume dilatancy stage ($Q > C^*$) under constant stress. Note that due to the natural variability between the specimens, determination of C^* based on the quasi-static stress-strain curves in Fig. 2 may differ from the true C^* of the specimens in stress-stepping creep tests. Fig. 4 depicts the sensitivity of minimum strain rate to stress in CFL. Regardless of the last stress step, the minimum strain rate of the specimens increased with increase of the deviatoric stress during the volume dilatancy stage. The minimum strain rate in the last stress step was much

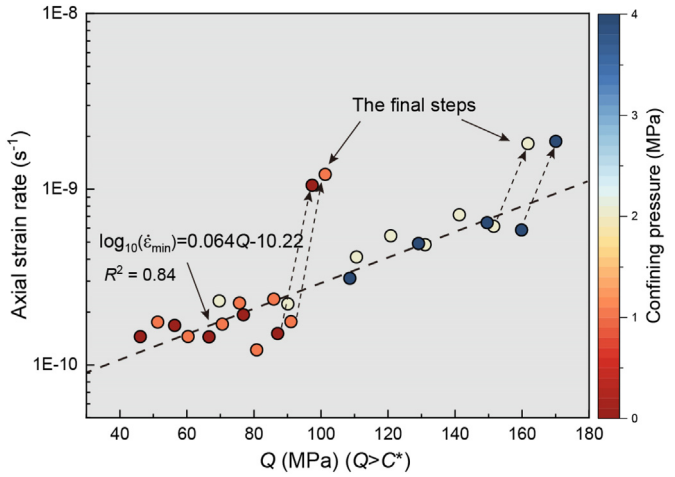

Fig. 4. The sensitivity of axial strain rate of CFL to axial stress. With respect to C^*, it varies with the confining pressure and structure of CRL and is determined according to the stress-strain curve in Fig. 2. The scatter points are the strain rate in secondary creep of every stress-step.

larger than those of the previous stress steps. The minimum strain rates in the last steps with increase of the confining pressure were 1.05×10^{-9} s^{-1}, 1.22×10^{-9} s^{-1}, 1.82×10^{-9} s^{-1}, and 1.87×10^{-9} s^{-1}, respectively. Therefore, the minimum strain rate of CRL was sensitive to stress and confining pressure. In addition, regardless of the last stepping loading, the logarithmic coordinate of the minimum strain rate had an approximately linear relationship with the deviatoric stress:

$$\log_{10}(\dot{\varepsilon}_{\min}) = 0.064Q - 10.22 \tag{1}$$

Eq. (1) could be rewritten as

$$\dot{\varepsilon}_{\min} = A \exp\left(\frac{Q}{\sigma^*}\right) \tag{2}$$

where Q and σ^* denote the deviatoric stress and activation stress, respectively.

The minimum axial strain rate $\dot{\varepsilon}_{\min}$ of CRL followed the power law evolution with deviatoric stress (see Eq. (2)). The activation stress of CFL was determined as 6.79 MPa, which was comparable to sandstone and porous limestone (Heap et al., 2009; Brantut et al., 2014a), and was significantly lower than that of 38 MPa of Tavel limestone in the semi-brittle zone (Nicolas et al., 2017).

Taking the stress-stepping creep test of CFL with a confining pressure of 4 MPa as an example, the compressive strain is defined as positive and the tensile strain is defined as negative (see Fig. 5), and the lateral creep strain was reset to zero for each step. Fig. 5a demonstrates that the lateral creep rate in the last step was significantly greater than these in previous creep steps, which is consistent with the trend of axial strain rate. The lateral strain in the last stress step experienced three creep stages. The minimum lateral strain rate in this step was 4.06×10^{-9} s^{-1} (Fig. 5b). It is worth noting that the lateral creep rate before the last step did not present an obvious deceleration process but a sudden decrease, and the $\dot{\varepsilon}_{\min}$ with deviatoric stress 88.15 MPa was in the same order of magnitude as the last step (Fig. 5b). At these steps with small deviatoric stresses (i.e. $Q < C^*$), the lateral strains of the specimen developed throughout the steady-state creep, and the considerable creep velocity in these stress steps indicated that the lateral strains seem not to converge (Fig. 5a). This phenomenon differed from the reported creep characteristics of conventional rock materials (Yang et al., 2014; Wang et al., 2021; Xue et al., 2022).

To understand the creep characteristics of CRL, the lateral and axial strain rates of steady creep in each step were extracted for comparison. CRLs presented the same creep trend under different confining pressures. The axial and lateral strain rates decreased first, indicating that the specimens underwent elastic compaction. As the deviatoric stresses increased, the strain rates increased rapidly after reaching the minimum, and many microcracks initiated and propagated within specimens, causing volume dilatancy. However, the lateral strain rates of the other specimens were significantly greater than the axial strain rates except for the specimen with a confining pressure of 1 MPa (see Fig. 6). The volume strain can be written as

$$\varepsilon_v(t) = \int [\dot{\varepsilon}_a(t) + 2\dot{\varepsilon}_l(t)]dt = \varepsilon_a(t) + 2\varepsilon_l(t) \tag{3}$$

$$\mu = \int \left|\frac{\dot{\varepsilon}_a(t)}{\dot{\varepsilon}_l(t)}\right| dt = \left|\frac{\varepsilon_a(t)}{\varepsilon_l(t)}\right| \tag{4}$$

where $\varepsilon_v(t)$, $\varepsilon_a(t)$ and $\varepsilon_l(t)$ denote the volumetric strain, axial strain, and lateral strain, respectively. The $\varepsilon_a(t)$ is positive and $\varepsilon_l(t)$ is negative. In addition, $\dot{\varepsilon}_a(t)$ and $\dot{\varepsilon}_l(t)$ denote the axial strain rate and lateral strain rate, respectively, and μ is the Poisson's ratio. According to Eq. (4), the lateral strain rate in steady creep stage is significantly greater than axial strain rate. Consequently, the Poisson's ratio of the specimen exceeded 1, which was impossible in the regime of continuous media.

In the regime of elasticity, the deformation of continuous materials is always constrained by the Poisson effect, and the Poisson's ratio is usually less than 0.5. However, Poisson's ratio of CRL in the elastic compression stage was significantly larger than 0.5, indicating that the dominant mechanism of creep deformation of CRL originated from a certain kind of structure inside the specimen rather than from the deformation and rheology of the continuous media. In this test, the Poisson's ratio of CRL subjected to quasi-static load ($\dot{\varepsilon}_a(t) \approx 10^{-5}$ s^{-1}) ranged from 0.23 to 0.34, while the Poisson's ratio of CRL during creep deformation (10^{-10} s$^{-1} < \dot{\varepsilon}_a(t) < 10^{-8}$ s^{-1}) was significantly larger than 0.5, indicating that the mechanism responsible for significantly larger lateral deformation was activated only in creep range. Thus, the creep deformation mechanism of CRL was different from that of quasi-static deformation, and the mechanism that dominated its lateral deformation was sensitive to strain rate and time. Furthermore, Eq. (3) indicates that the axial strain rate was less than twice the lateral strain rate in the steady creep stage, implying that the specimen was in a state of volumetric dilatancy and was independent of the magnitude of deviatoric stress Q.

3.4. Microstructure

The CT scanning slice and petrographic thin section were utilized to investigate the micro-mechanical behaviors of CRL under constant stress preliminarily. Coral reefs were rocky bodies of the calcareous skeletons of reef-building corals, accumulated with calcareous organisms, such as coralline algae, mollusks, and foraminifera. The CRL specimens in triaxial creep tests mainly encountered shear failure (Fig. 7a), and the tensile microcracks were extensively distributed near the shear zone, indicating that the cracking mechanism during the microcrack initiation and propagation was mainly Mode-I tensile fracture (Fig. 7b(I) to 7b (VI)). The coral skeleton was the mechanically stronger part of CRL (Fig. 8c and d). In comparison, the foraminiferal cementation zone in Fig. 8a is the mechanically weaker part of CRL, and the polarizing

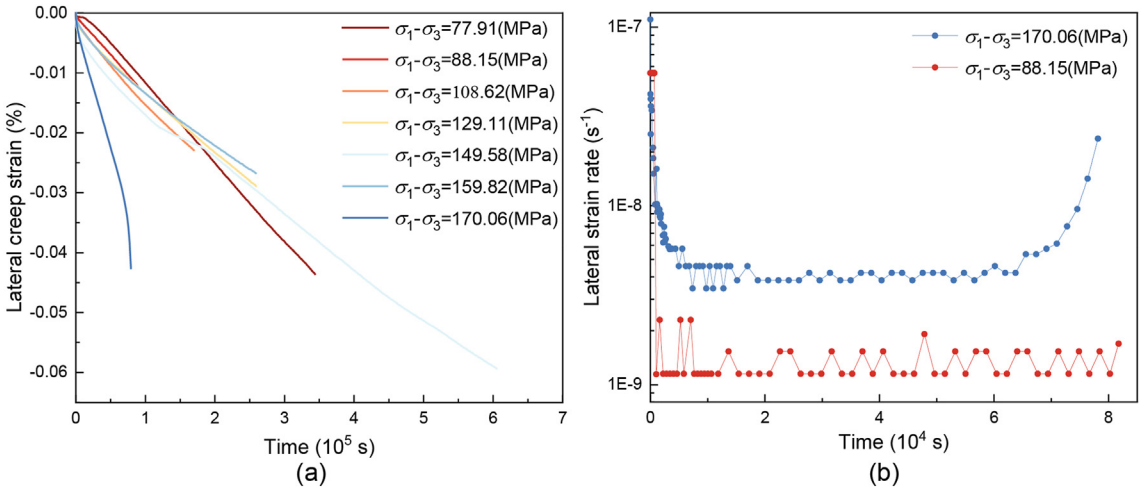

Fig. 5. The deformation characteristics of lateral creep of CFL (confining pressure is 4 MPa): (a) includes all curves of lateral creep strain versus time during the stress-stepping, and (b) is the comparison analysis of lateral strain rate during creep processes when the constant deviatoric stresses are 88.15 MPa and 170.06 MPa, respectively.

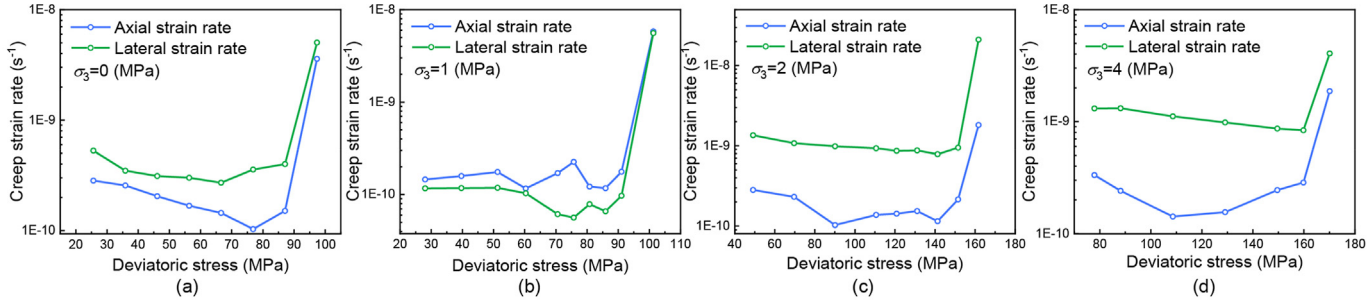

Fig. 6. The evolution processes of creep strain rate with respect to deviatoric stress of CFL. (a), (b), (c), and (d) correspond to the confining pressures of 0 MPa, 1 MPa, 2 MPa, and 4 MPa, respectively.

microscope observations indicated that crack initiation was mainly distributed in this zone. Sparry calcite crystals contained a large number of intergranular cracks, intragranular cracks, and transgranular cracks. The plastic behaviors of crystals were one of the important sources of creep deformation (Fig. 8a).

Note that the crystal microcrack, tension fracture, and grain fragmentation in Fig. 8a–d are all creep-induced plastic deformations rather than quasi-static loading and final failure. The stress concentration easily appeared around the pores of the specimen, and cracking within the grains occurred when the crystals were unable to withstand greater plastic strain. This viewpoint is also verified by the intracrystalline cracks of sparry calcite cemented by medium-thick annular edges (Fig. 9b). The water in the saturated specimens is a non-saturated solution for $CaCO_3$ (Brantut et al., 2014a; Nicolas et al., 2017), which promotes creep behaviors such as pressure dissolution and stress corrosion. It is difficult to quantify the contribution of pressure dissolution to creep in this experiment, but pressure dissolution is indeed observed in Fig. 8b. Moreover, the pore distribution area of the coral skeleton is also a highly concentrated region of the stress field, and coral branches experience tensile fracture and grain crush in the brittle creep regime (see Fig. 8c and d). Therefore, polarizing microscope observation revealed that the brittle creep mechanisms of CRL under constant stress included plastic deformation of crystal, grain crush, pressure dissolution of calcite, and crystal cracking. However, the above microscopic mechanisms of brittle creep cannot explain the significantly large lateral creep rate.

4. Discussion

4.1. Rate sensitivity of deformation mechanisms

The comparison of lateral and axial strain rates in Fig. 6 demonstrates that the dominant mechanism of lateral deformation in CRL was sensitive to the strain rate, and the Poisson effect did not constrain the lateral and axial creep deformations. Fig. 9 compares the stress-strain curve characteristics of the stepping creep of CRL and Tavel limestone to further investigate the significantly large lateral deformation of CRL in the brittle creep. The analysis demonstrated that the specimens underwent volumetric dilatancy at the end of creep, which was independent of the volumetric compaction and dilatancy of the specimens during quasi-static loading (Fig. 9a). The stress-stepping creep tests of Tavel limestone with confining pressures of 55 MPa and 70 MPa fell into the regimes of brittle and semi-brittle, respectively (Nicolas et al., 2017). However, the Tavel limestone experienced volumetric compaction in stress-stepping creep tests when the average stress Q_m was less than the critical transition stress C^*, while the Tavel limestone encountered volumetric dilatancy when Q_m was greater than C^* (Fig. 9b). Therefore, the trend of volumetric deformation in stress-stepping creep of Tavel limestone was consistent with that in quasi-static loading. The main mineral compositions of both the CRL and Tavel limestone were calcite, and the stress-stepping creep tests were both in a brittle regime, while the volumetric deformation trend of specimen creep with Q_m less than C^* was

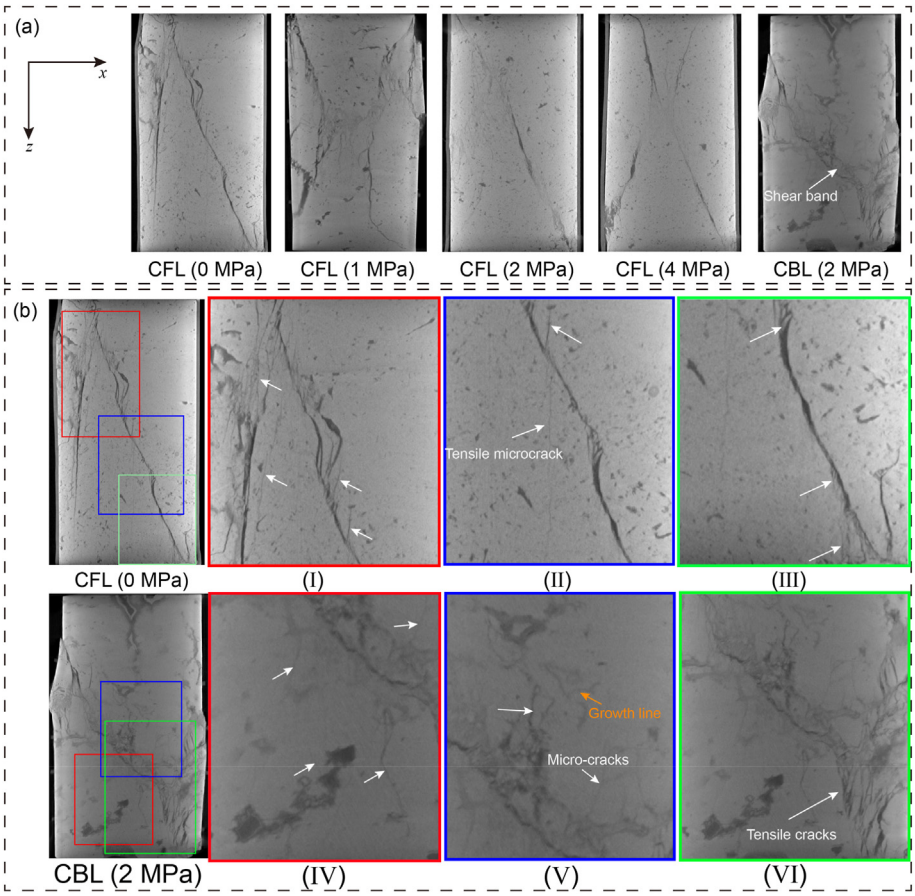

Fig. 7. Failure pattern analysis of creep deformation: (a) depicts tensile-shear mixed failure, single shear failure, and conjugate shear failure in CFL and CBL, and (b-I) to (b-VI) represent typical micro-cracking mechanism in CFL and CBL.

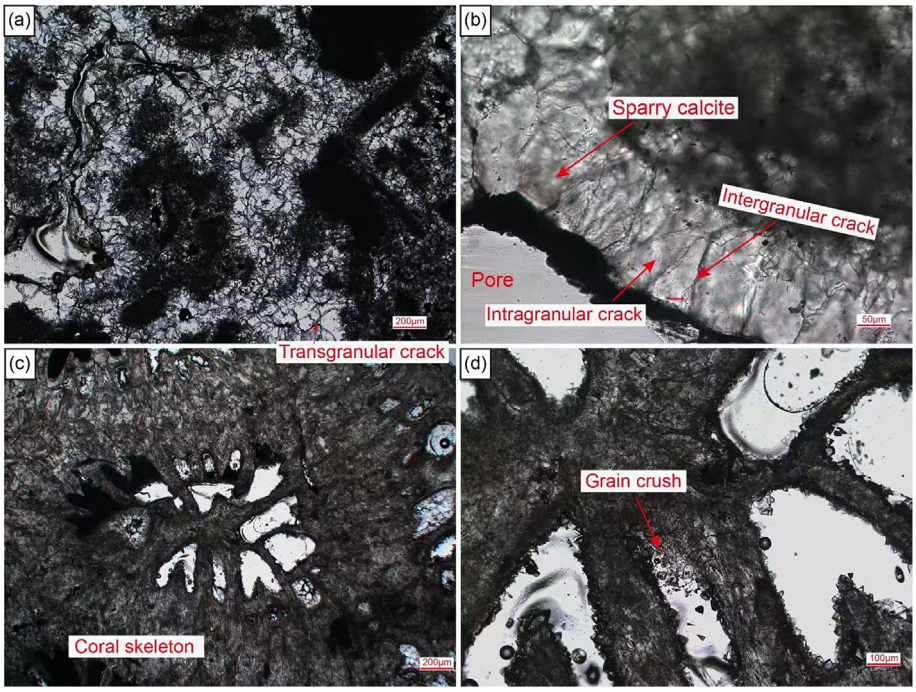

Fig. 8. The micromechanical creep behaviors of crystal gains observed by petrographic thin section: (a) the cemented foraminiferan; (b) the equal-thickness rim-cemented columnar calcite; and (c) and (d) the limestone skeleton of scleractinian coral.

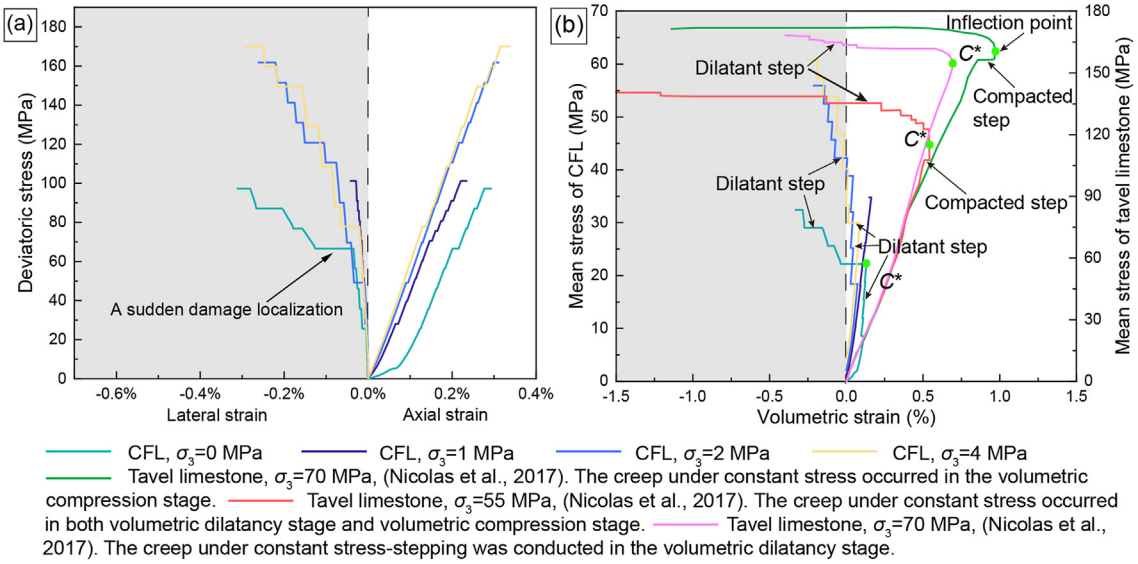

Fig. 9. The stress-strain relationships subjected to stress-stepping loading: (a) the deviatoric stresses as functions of strains for CFL samples subjected to different confining pressures, and (b) the mean stresses as functions of volumetric strains for CFL and Tavel limestone.

completely opposite.

The volumetric evolution of the Tavel limestone at a confining pressure of 55 MPa was emphasized. The deviatoric stress was first loaded to a target value Q_1 ($Q_1 < C^*$) at a constant strain rate ($\approx 10^{-5}$ s^{-1}). The specimen underwent elastic deformation after initial crack closure. Subsequently, the specimen occurred creep deformation at constant stress, and the volume was further compacted (see Fig. 9b). The specimen underwent a transition from volumetric compaction to volumetric dilatancy (critical transition pressure C^*) during loading to the next target stress using a constant strain rate. The internal state of the specimen experienced microcrack initiation and dilatancy during this transition. Subsequently, the specimen underwent volumetric dilatancy in all creep steps (Fig. 9b). The change in the internal state of the specimen from volumetric compaction to volumetric dilatancy was only the microcrack propagation throughout the loading process. Therefore, the real core of controlling volumetric compaction to volumetric dilatancy lied in the content of internal microcracks. Microcrack was a structure within the specimen that caused the specimen to change from continuous to discontinuous, which was the underlying reason for volumetric dilatancy of the specimen in quasi-static and creep deformations. This deduction implied that microstructures were extensively present in the CRL (e.g. microcracks, primary pores, or other primary flaws), and were named 'microdefect' thereafter in this paper. The deformability of this microdefect exhibited a dormant state under quasi-static loading and was activated under constant stress. Therefore, the next step is to find out exactly which microdefect is responsible for the abovementioned abnormal phenomenon.

4.2. Underlying competition mechanism

An interesting phenomenon in deviatoric stress-strain curves help us to further understand the micro-mechanisms involved in the creep process of CRL (Fig. 10a). After each quasi-static loading to the target stress, a bulge appears at the right of curve. The time series is correlated with a color bar in the enlarged figure of Fig. 10a—and a typical stage is colored with this color bar. The results revealed that after completion of the quasi-static loading, the curves moved in a positive direction and then in a negative

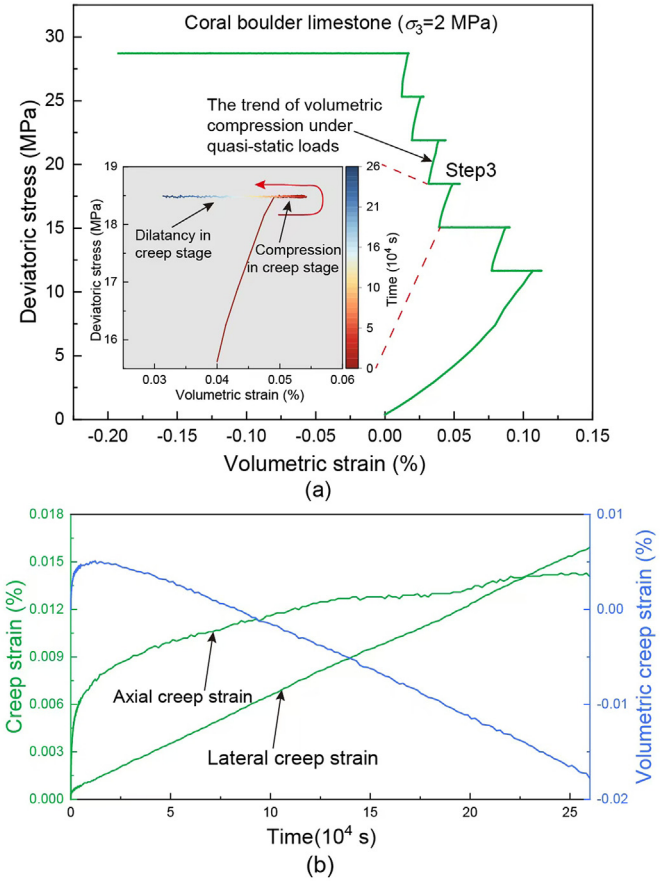

Fig. 10. The competition mechanism of creep deformations in CRL samples: (a) the deviatoric stress as a function of volumetric strain in CBL, and (b) the strain evolution in a typical creep stage.

direction in the creep state. This indicates that the specimen underwent volumetric compaction at the beginning of this creep step, followed by volumetric dilatancy. This phenomenon suggested that

there was competition between different creep mechanisms within the specimen. Generally, conventional micro-mechanisms, such as crystal deformation, dislocations, particle fragmentation, pressure dissolution, and stress corrosion, caused volumetric compaction of specimen when Q was less than C^* (Nicolas et al., 2017). However, the rheology of the microdefect within CRL caused the specimen to undergo volumetric dilatancy when Q was less than C^*. Therefore, there was a competition between the rheology of the microdefect and the conventional microscopic creep mechanism. Fig. 10b exhibits this competitive process. In Fig. 10b, both the axial and lateral strains are set to positive and the initial strain are set to zero for demonstration purpose. It was obvious that these two deformations were independent of each other. The axial strain exhibited distinct instantaneous creep and steady creep stages, while the lateral creep strain always grew linearly at a constant rate. Both the lateral and axial deformations of the specimen experienced conventional instantaneous creep and steady creep stages when conventional microscopic creep mechanism dominated. The lateral strain of the specimen grew linearly over elapsed time at a constant rate when the microdefect rheology dominated. The competition of creep mechanisms within the specimen resulted in volumetric compaction, followed by volumetric dilatancy.

4.3. Dominant creep micro-mechanism

Fig. 8 depicts the evidence left by creep in the microstructure of CRL, elaborating on the traditional micro-mechanisms of crystal cracking, pressure dissolution, particle crush, and plastic deformation. These micro-mechanisms were also observed in limestone creep (Brantut et al., 2014a, 2014b; Nicolas et al., 2017). However, initial pores and microcracks, which are also common in porous limestone, are not dominant microscopic factors in the lateral creep deformation of CRL. Fig. 11 shows the crack propagation behaviors within CRL. The macroscopic cracks in Fig. 11a start to extend from the two tips of the elongated biopore in the center and then penetrate through the pores on both sides when the specimen fails. Furthermore, the crack propagation mode was Type I tension crack. Similar stress concentration and tip crack propagation are also presented in Fig. 11b and d. In addition, the macroscopic cracks in Fig. 11c propagate in the coralline algae cemented by sparry calcite with bifurcation cracks. These macroscopic cracks were produced when the specimen underwent brittle failure, while the creep process produced microscopic cracks.

Figs. 11e and 1 illustrates a large number of intracrystalline and transcrystalline cleavages, which are densely distributed and have the same orientation. This type of cleavage is produced during the crystallization of $CaCO_3$ in the seawater environment to form calcite, and it is commonly found in calcite deposited in the marine phase. The same orientation and extensive existence of cleavage in Fig. 11e and f are unique to CRL. Therefore, it is assumed that the cleavage was the microdefect dominating the lateral creep deformation of CRL. To verify this, several tensile rupture surfaces are visually observed. The results reveal that there are several locally smooth cleavage surfaces on the tension rupture surfaces (see Fig. 12a). The pore deformation, microcrack initiation and propagation under quasi-static load condition dominated the deformation of specimen, while the cleavage surface had no enough time to deform under a higher loading rate ($\dot{\varepsilon}_a(t) \approx 10^{-5}\ s^{-1}$). When the specimen was subjected to constant stress, the sliding mechanism of cleavage surface was activated and the specimen produced abnormal lateral creep deformation. In addition, the lateral creep deformation in Fig. 10b is approximately linear with elapsed time except for the last creep stage, which is the strong evidence of the sliding mechanism of cleavage surface dominating the lateral creep. Since linear deformation behavior occurs only with sliding, the traditional elastoplastic deformation of rock materials is nonlinear. To further verify this, the tensile and shear rupture surfaces in the failure specimen are selected to observe the crystal morphology by SEM, and they are also compared with the tensile rupture surfaces of the red sandstone in this paper, and the results are shown in Fig. 12.

As demonstrated in Fig. 12b–d, there are widely distributed

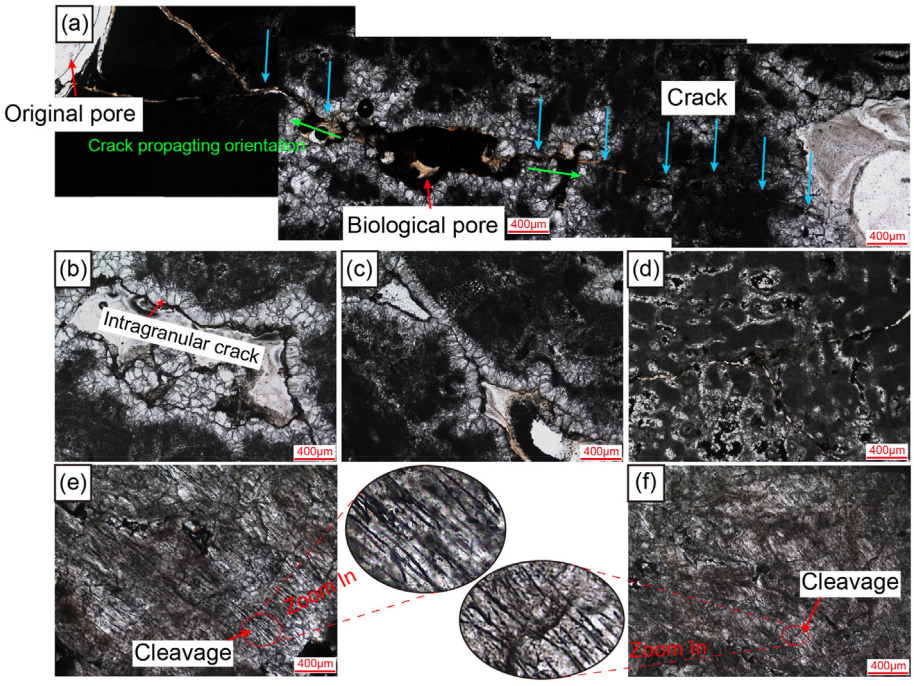

Fig. 11. Observation of petrographic thin sections by optical polarizing light microscope: (a), (b), and (c) macroscopic cracks propagate in pore tips; (d) macroscopic cracks propagate in Corallina officinalis; and (e) and (f) intragranular cleavages in calcite.

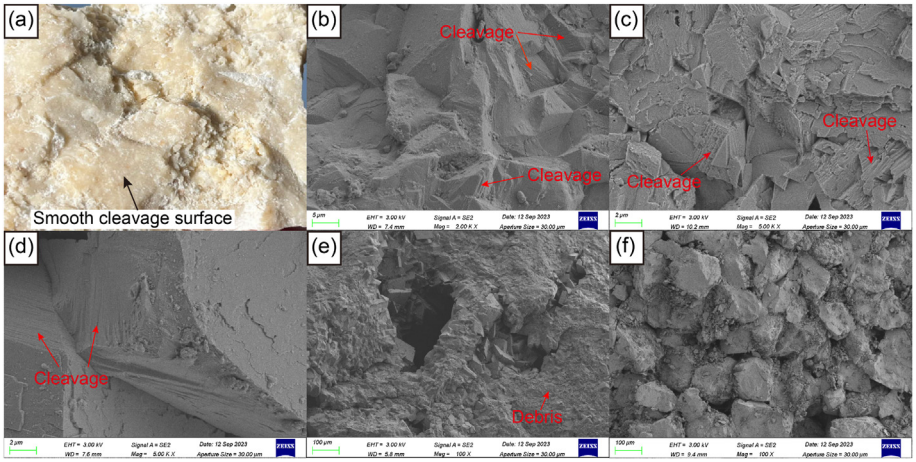

Fig. 12. Shapes on the failure surface: (a) tensile rupture surface of CRL; (b), (c), (d) SEM images of tensile rupture surface of CRL; (e) SEM image of shear band of CRL; and (f) SEM image of tensile rupture of sandstone.

regular lines inside the crystals, namely intracrystalline cleavage, which correspond to the cleavages in Fig. 11e and 12f. Tensile fracture perfectly represented intracrystalline cleavage within calcite. Furthermore, the creep deformation of CRL increased linearly over time only in the lateral direction, indicating that the cleavage surfaces in the calcite crystals presented a preferential distribution orientation. Calcite belonged to the trigonal system, and the relatively low CO2-3 concentration and high Ca^{2+} concentration in seawater promoted rapid calcite growth along the c-axis, resulting in the formation of elongated columnar crystals (Stanley et al., 2002; Steiner et al., 2018; Adams et al., 2023). The predominance of growth in the c-axis direction promoted the formation of cleavage surfaces in the crystals that were perpendicular to c-axis, such as the (010) crystal face (Bentov et al., 2009; Fitzer et al., 2014; Subhas et al., 2017). In the standing water environment of a lagoon and the flowing environment of seawater, the c-axis usually represented a vertical or tilted vertical orientation distribution, namely a horizontal or tilted horizontal orientation distribution of cleavage surface (Subhas et al., 2017; Liu et al., 2018; Steiner et al., 2018; Berg et al., 2019). Thus, the preferential growth of calcite in marine phase along the c-axis modulated the crystal shape, which influenced and oriented calcite cleavage formation with a statistically preferred distribution orientation. Moreover, the cleavages also existed in crystals of terrestrial rocks, such as marble, sandstone, gabbro, and dolomite, but the distribution of cleavage orientations was random (Zhang and Zhao, 2014), which explained why the lateral linear creep properties of CRL were significantly different from those of conventional terrestrial rocks.

The intracrystalline cleavage was the weak surface inside the crystal. The deformation of the intracrystalline cleavage was not obvious under quasi-static loading condition, which was masked by the deformation of microcracks and primary pores. The rheological mechanism of the intracrystalline cleavage was activated in the creep state, and its dominant slipping mechanism led to a significant increase in the lateral creep deformation. Compared with the smooth tensile rupture surface, the crystals on the tensile fracture surface of sandstone were intact, and the surface roughness was significantly higher than that of the CRL, indicating that the tensile cracks were all intergranular cracks. There were no weak surfaces within the crystals of red sandstone as in the case of intracrystalline cleavage (see Fig. 12f). Therefore, the comparative analysis of Figs. 11 and 12 confirms that calcite cleavage (including intracrystalline cleavage and transgranular cleavage) of marine diagenesis is the microdefect that dominates the lateral creep deformation of CRL. The sliding mechanism of the cleavage surface was activated in the creep state, which led to a significant increase in lateral creep deformation and volumetric dilatancy. The sliding mechanism of cleavage surface competed with the conventional microscopic creep mechanism. The lateral deformation of the specimen was dominated by the sliding mechanism of the cleavage, and the lateral strain developed linearly at low deviatoric stress levels. When the deviatoric stress Q was larger than C^*, the lateral deformation of the specimen was dominated by the conventional microscopic creep mechanisms, and the lateral strain exhibited the classical instantaneous creep, steady creep, and accelerated creep. The transition pressure of the dominant competing mechanism needed to be further investigated. And the volumetric dilatancy and volumetric compaction of the CRL were the integration of lateral and axial strains. At lower stress levels, lateral creep deformation significantly surpasses axial deformation. In the pile foundations of CRL strata, it is imperative to consider eccentric loads induced by lateral creep slipping. However, the volumetric dilatancy observed in the creep regime of CRL do not inherently pose a disadvantage for underground rock engineering endeavors. Consequently, there is a critical need to pay close attention to the forecasting of creep deformation within slopes and pile foundations.

4.4. Creep constitutive model of CRL

Given the unique competing mechanism in the creep process of CRL, this study further developed a creep constitutive model for CRL. Since the axial and lateral creep behaviors were mutually independent, this study first divided the creep deformation of CRL into axial and lateral directions to establish separate constitutive equations, and then integrated the axial and lateral creep deformations. Among them, the axial creep behaviors were similar to those of conventional rocks. The specimen underwent obvious instantaneous creep and steady creep at each step of creep loading except the last step. For axial deformation, this study adopted the classical Burgers model for parameter calibration without any hesitation. Fig. 3c, 5a and 10b reveal that the lateral creep of the specimen grows approximately linearly with time in the early stage. The conventional microscopic creep mechanisms only dominated the lateral creep deformation at a high deviatoric stress level. Thus, the lateral creep rate depends on the deviatoric stress level (see Fig. 6), which greatly contributes to determining the form of creep constitutive model for lateral direction. The creep characteristics of CRL and conventional rocks were similar at the last

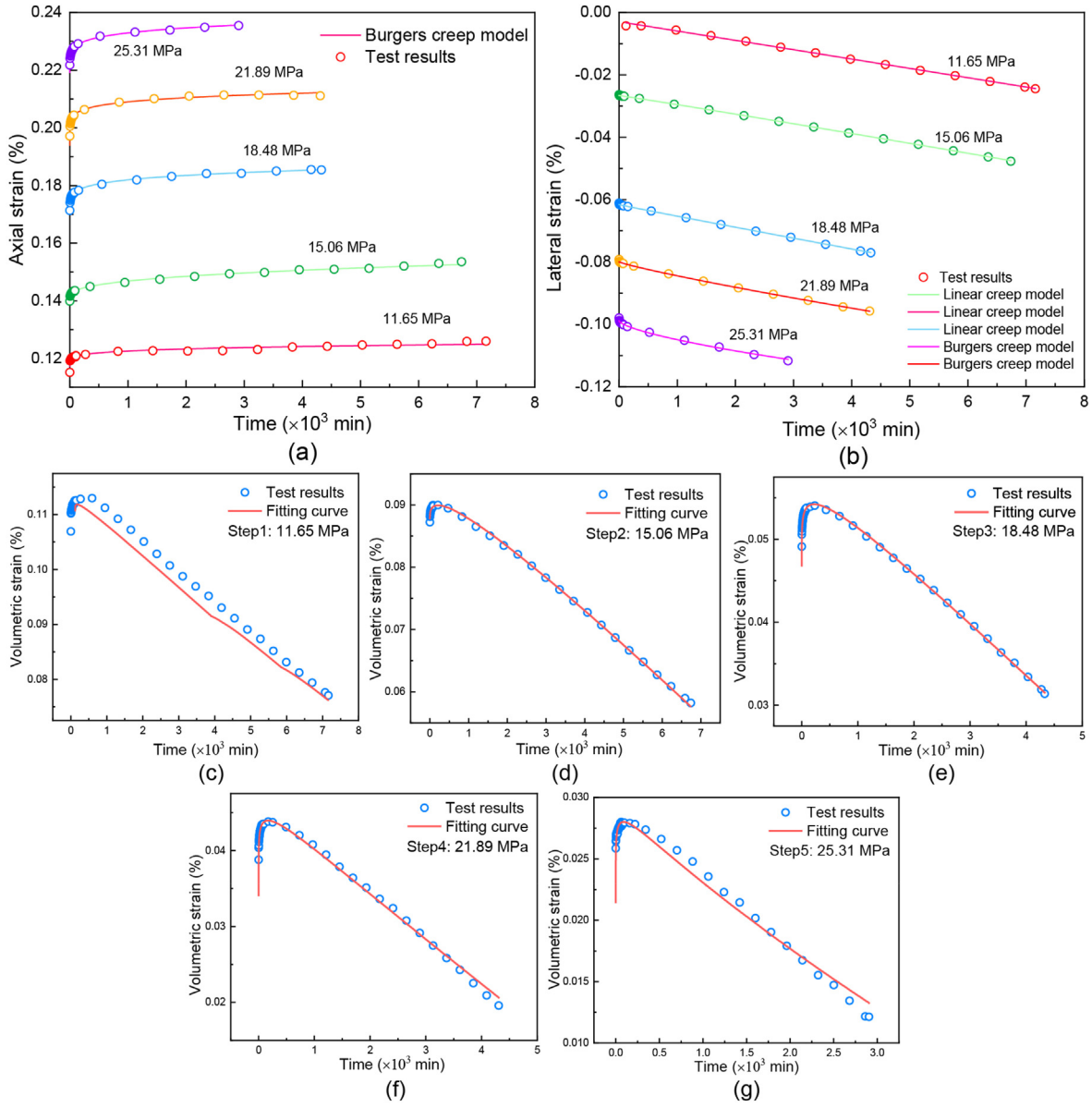

Fig. 13. Validation of creep model: (a) creep model validation of axial strain; (b) creep model validation of lateral strain; (c), (d), (e), (f), and (g) are the creep model validations of volumetric strain.

step, thus, only the creep processes before the last step were considered.

Since anisotropy in the material was not considered, the Burgers model was represented in the form of the tensor. This study considered only the axial strain and reduced the Burgers model to a one-dimensional form:

$$\varepsilon_{11}(t)=\frac{S_{11}}{2G_1}+\frac{S_{11}}{2\eta_1}t+\frac{S_{11}}{2G_2}\left[1-\exp\left(\frac{G_2}{\eta_2}\right)t\right] \tag{5}$$

where $\varepsilon_{11}(t)$ and S_{11} denote axial strain and component of deviatoric stress, respectively; G_1 and G_2 are the instantaneous shear modulus and viscoelastic shear modulus, respectively; η_1 and η_2 are the viscosity coefficients.

This paper utilized the damage variable D_σ to characterize the internal state of specimen during the creep process. The D_σ is a function of axial deviatoric stress level. The lateral creep deformation was dominated by slipping mechanism of cleavage at a low deviatoric stress level, and it was dominated by conventional microscopic creep mechanisms at a high deviatoric stress level. The damage variable D_σ is given by

$$D_\sigma=1-\mathrm{e}^{-aS_{11}}\ (a>0) \tag{6}$$

According to the characteristics of lateral creep, the lateral creep deformation of CRL can be described by

$$\varepsilon_{33}(t)=(1-D_\sigma)(b+ct)+D_\sigma\left\{\frac{S_{33}}{2G_1}+\frac{S_{33}}{2\eta_1}t+\frac{S_{33}}{2G_2}\left[1-\exp\left(\frac{G_2}{\eta_2}\right)t\right]\right\} \tag{7}$$

$$\varepsilon_{\mathrm{v}}(t)=\varepsilon_{11}(t)+2\varepsilon_{33}(t) \tag{8}$$

where a, b, and c denote the model parameters; S_{33} denotes the component of deviatoric stress; and $\varepsilon_{\mathrm{v}}(t)$ is volumetric strain.

Eq. (7) describes the competition mechanism in the lateral creep

of CRL well. Fig. 13a and b verifies the creep model for axial strain and lateral strain, respectively, and Fig. 13c–g verifies the validity of Eq. (8) for volumetric strain calculation. It seems that the proposed creep model lays a theoretical foundation for prediction of the long-term deformation of coral reefs.

5. Conclusions

This paper revealed for the first time the unique microscopic mechanism in time-dependent deformation of CRL based on a series of triaxial tests under constant strain rate and constant stress in conjunction with microscopic probing means, and finally proposed a constitutive model. The main conclusions can be drawn as follows:

(1) In the brittle regime, the minimum strain rate of axial creep of CRL is sensitive to stress and insensitive to confining pressure. When the deviatoric stress Q is greater than the critical stress C^*, the minimum axial strain rate $\dot{\varepsilon}_{\min}$ follows a power function evolution with the deviatoric stress Q.
(2) The sliding mechanism of cleavage surface is distinctive to CRL in marine sedimentation. This sliding mechanism of cleavage surface competes with the conventional rheology micro-mechanisms. In a lower deviatoric stress level, the lateral deformation of the specimen is dominated by the sliding mechanism, and the lateral strain develops linearly. When the deviatoric stress Q is greater than C^*, the lateral deformation is dominated by the conventional rheology micro-mechanisms, and the lateral strain exhibits the classical primary creep, steady creep, and tertiary creep processes.
(3) The sliding mechanism of cleavage surface that dominates the lateral deformation of CRL is sensitive to strain rate and time. This mechanism is activated only in the creep regime (i.e. strain rate less than 10^{-5} s^{-1}), and the anomalous lateral creep deformation arises. The CRL exhibits deformation discordance in axial and lateral creep strains due to the sliding mechanism of cleavage surface.
(4) Based on the microscopic creep mechanisms of CRL, a creep constitutive model is proposed in this paper to describe the properties of axial and lateral creep deformations of CRL. It can characterize the relationships in the microscopic creep mechanisms. This constitutive model provides a reference for the long-term stability assessment of engineering structures in island reefs.

CRediT authorship contribution statement

Kai Wu: Conceptualization, Data curation, Formal analysis, Investigation, Software, Validation, Visualization, Writing – original draft, Writing – review & editing. **Qingshan Meng:** Formal analysis, Funding acquisition, Methodology, Project administration, Resources. **Le Luo:** Data curation, Methodology, Visualization. **Qinglong Qin:** Methodology, Resources. **Chi Wang:** Formal analysis, Writing – review & editing. **Xinzhi Wang:** Methodology, Project administration, Resources. **Tianli Shen:** Conceptualization, Methodology. **Haozhen Ding:** Validation, Writing – review & editing.

Declaration of competing interest

The authors declare that they have no known competing financial interests or personal relationships that could have appeared to influence the work reported in this paper.

Acknowledgements

This research is supported by the National Natural Science Foundation of China (Grant Nos. 41877267, 41877260), the Priority Research Program of the Chinese Academy of Science (Grant No. XDA13010201).

References

Adams, A., Daval, D., Baumgartner, L.P., Bernard, S., Vennemann, T., Cisneros-Lazaro, D., 2023. Rapid grain boundary diffusion in foraminifera tests biases paleotemperature records. Commun. Earth Environ. 4, 1–11.
Baud, P., Schubnel, A., Wong, T., 2000. Dilatancy, compaction, and failure mode in Solnhofen limestone. J. Geophys. Res. Solid Earth 105, 19289–19303.
Bentov, S., Brownlee, C., Erez, J., 2009. The role of seawater endocytosis in the biomineralization process in calcareous foraminifera. Proc. Natl. Acad. Sci. USA 106, 21500–21504.
Berg, R.D., Solomon, E.A., Teng, F.Z., 2019. The role of marine sediment diagenesis in the modern oceanic magnesium cycle. Nat. Commun. 10, 4371.
Brantut, N., Baud, P., Heap, M.J., 2012. Meredith PG. Micromechanics of brittle creep in rocks. J. Geophys. Res. Solid Earth 117, 9299.
Brantut, N., Heap, M.J., Baud, P., Meredith, P.G., 2014a. Mechanisms of time-dependent deformation in porous limestone. J. Geophys. Res. Solid Earth 119, 5444–5463.
Brantut, N., Heap, M.J., Baud, P., Meredith, P.G., 2014b. Rate- and strain-dependent brittle deformation of rocks. J. Geophys. Res. Solid Earth 119, 1818–1836.
Cheng, H., Zhang, Y., Zhou, X., 2021. Nonlinear creep model for rocks considering damage evolution based on the modified Nishihara model. Int. J. GeoMech. 21, 2071.
Cong, L., Hu, X., 2017. Triaxial rheological property of sandstone under low confining pressure. Eng. Geol. 231, 45–55.
Effenberger, C., Kressner, D., 2012. Chebyshev interpolation for nonlinear eigenvalue problems. BIT. Numer. Math 52, 933–951.
Evans, B., Fredrich, J.T., Wong, T.F., 1990. The brittle-ductile transition in rocks: recent experimental and theoretical progress. In: Brittle-Ductile Transit. Rocks. American Geophysical Union (AGU), pp. 1–20.
Fang, Z., Jia, Y., Wu, W., 2023. Forecasting the occurrence of injection-induced heterogeneous slip on rock fractures. Eng. Geol. 325, 107291.
Fitzer, S.C., Phoenix, V.R., Cusack, M., Kamenos, N.A., 2014. Ocean acidification impacts mussel control on biomineralisation. Sci. Rep. 4, 6218.
GB/T 50218-2014, 2015. Standard for Engineering Classification of Rock Mass. China Planning Press, Beijing, China (in Chinese).
Gove, J.M., Williams, G.J., Lecky, J., Brown, E., Conklin, E., Counsell, C., 2023. Coral reefs benefit from reduced land–sea impacts under ocean warming. Nature 621, 536–542.
Guppy, H.B., 1889. The structure and distribution of coral reefs. Nature 40, 102–102.
Guppy, H.B., 1882. On Coral-eating habits of holothurians. Nature 27, 7–8.
Huang, D., Zhang, Z., Lin, X., Li, H., 2014. Fractal characteristics of mudstone microscopic morphology in MATLAB environment. In: The Taishan Academic Forum – Project on Mine Disaster Prevention and Control. Atlantis Press, pp. 161–166.
Heap, M.J., Baud, P., Meredith, P.G., 2009. Influence of temperature on brittle creep in sandstones. Geophys. Res. Lett. 36, L19305.
Heard, H.C., 1960. Chapter 7: transition from brittle fracture to ductile flow in Solenhofen limestone as a function of temperature, confining pressure, and interstitial fluid pressure. In: Griggs, D., Handin, J. (Eds.), Rock Deform. Symp., vol. 79. Geological Society of America.
Liteanu, E., Spiers, C.J., Bresser, J.H.P. de, 2013. The influence of water and supercritical CO_2 on the failure behavior of chalk. Tectonophysics 599, 157–169.
Liu, Y.W., Eagle, R.A., Aciego, S.M., Gilmore, R.E., Ries, J.B., 2018. A coastal coccolithophore maintains pH homeostasis and switches carbon sources in response to ocean acidification. Nat. Commun. 9, 2857.
Maranini, E., Yamaguchi, T., 2001. A non-associated viscoplastic model for the behaviour of granite in triaxial compression. Mech. Mater. 33, 283–293.
Meng, Q.S., Wu, K., Zhao, Y., Luo, L., Li, X., Wang, C., Zhong, Y., Shen, T.L., 2024. Dynamic compressive properties and self-similarity characteristics of deep coral reef limestone subjected to high loading rates. J. Build. Eng. 86, 108853.
Meng, Q.S., Wu, K., Zhou, H.R., Qin, Q.L., Wang, C., 2022. Mesoscopic damage evolution of coral reef limestone based on real-time CT scanning. Eng. Geol. 307, 106781.
Nicolas, A., Fortin, J., Regnet, J.B., Verberne, B.A., Plümper, O., Dimanov, A., 2017. Brittle and semibrittle creep of Tavel limestone deformed at room temperature. J. Geophys. Res. Solid Earth 122, 4436–4459.
Roberts, L.A., Buchholz, S.A., Mellegard, K.D., Düsterloh, U., 2015. Cyclic loading effects on the creep and dilation of salt rock. Rock Mech. Rock Eng. 48, 2581–2590.
Stanley, S.M., Ries, J.B., Hardie, L.A., 2002. Low-magnesium calcite produced by coralline algae in seawater of Late Cretaceous composition. Proc. Natl. Acad. Sci. USA 99, 15323–15326.
Steiner, Z., Turchyn, A.V., Harpaz, E., Silverman, J., 2018. Water chemistry reveals a significant decline in coral calcification rates in the southern Red Sea. Nat. Commun. 9, 3615.

Subhas, A.V., Adkins, J.F., Rollins, N.E., Naviaux, J., Erez, J., Berelson, W.M., 2017. Catalysis and chemical mechanisms of calcite dissolution in seawater. Proc. Natl. Acad. Sci. USA 114, 8175–8180.
Tang, Q., Zhang, J., Feng, Y., Li, J., Yao, Y., Sun, J., Zhan, W., 2018. Numerical simulation for shallow strata stability of coral reef in the southwest of Yongshu Reef (South China Sea). J. Ocean Univ. China 17, 763–772.
Ulusay, R., 2015. The ISRM Suggested Methods for Rock Characterization, Testing and Monitoring: 2007-2014. Springer International Publishing, Cham.
Wang, Y., Cong, L., Yin, X., Yang, X., Zhang, B., Xiong, W., 2021. Creep behaviour of saturated purple mudstone under triaxial compression. Eng. Geol. 288, 106159.
Weidinger, P., Hampel, A., Blum, W., Hunsche, U., 1997. Creep behaviour of natural rock salt and its description with the composite model. Mater. Sci. Eng., A 234–236, 646–648.
Wong, T., Baud, P., 2012. The brittle-ductile transition in porous rock: a review. J. Struct. Geol. 44, 25–53.
Wu, J., Fu, H., Zhang, L., Zhang, X., Guo, D., 2022. Stability analysis of surrounding rock in underground chamber excavation of coral reef limestone. Rock Mech. Rock Eng. 55, 4717–4742.
Wu, K., Meng, Q.S., Li, R.X., Luo, L., Ke, Q., Wang, C., 2023a. A machine learning-based strategy for predicting the mechanical strength of coral reef limestone using X-ray computed tomography. J. Rock Mech. Geotech. Eng. 15, 124–138.
Wu, K., Meng, Q.S., Qin, Q.L., Jiang, X., Wang, C., 2022a. Microscopic mechanisms of coral reef limestone crack propagation. Mar. Georesour. Geotechnol. 0, 1–15.
Wu, K., Meng, Q.S., Wang, C., Qin, Q.L., Li, C.S., 2023b. Experimental investigation of damage evolution characteristics of coral reef limestone based on acoustic emission and digital volume correlation techniques. Rock Mech. Rock Eng. 56, 2357–2374.
Wu, K., Meng, Q.S., Wang, C., Qin, Q.L., Dong, Z.W., 2022b. Investigation of damage characteristics of coral reef limestone under uniaxial compression based on pore structure. Eng. Geol. 313, 106976.
Xue, Y., Xu, T., Heap, M.J., Meredith, P., Mitchell, T., Wasantha, P.L.P., 2022. Time-dependent cracking and brittle creep in macrofractured sandstone. Int. J. Rock Mech. Min. Sci. 162.
Yang, C., Daemen, J.J.K., Yin, J.H., 1999. Experimental investigation of creep behavior of salt rock. Int. J. Rock Mech. Min. Sci. 36, 233–242.
Yang, S.Q., Jing, H.W., Cheng, L., 2014. Influences of pore pressure on short-term and creep mechanical behavior of red sandstone. Eng. Geol. 179, 10–23.
Zhang, Q., Yang, W., Chen, F., Li, W., Wang, J., 2011. Long-term strength and microscopic failure mechanism of hard brittle rocks. Chin. J. Geotech. Eng. 33, 1910–1918 (in Chinese).
Zhang, Q.B., Zhao, J., 2014. Quasi-static and dynamic fracture behaviour of rock materials: phenomena and mechanisms. Int. J. Fract. 189, 1–32.
Zhang, X., Spiers, C.J., Peach, C.J., 2010. Compaction creep of wet granular calcite by pressure solution at 28 °C to 150 °C. J. Geophys. Res. Solid Earth 115, B9.
Zhao, H.T., Sha, Q.A., Zhu, Y.Z., 1992. Quaternary Coral Reef Geology of Yongshu Reef, Nansha Islands. Ocean Press, Beijing (in Chinese).
Zhao, J., Feng, X.T., Zhang, X., Yang, C., 2019. Brittle and ductile creep behavior of Jinping marble under true triaxial stress. Eng. Geol. 258, 105157.
Zheng, K., Meng, Q.S., Wang, R., Yu, J., Wu, W., Yu, K., 2020. Advances in study of engineering geological characteristics of coral reef limestone. Mar. Geol. Quat. Geol. 40, 42–49 (in Chinese).
Zhang, Y., Deng, Z., Chen, P., Luo, H., Zhang, R., Yu, C., Zhan, C., 2022a. Experimental and numerical analysis of pile–rock interaction characteristics of steel pipe piles penetrating into coral reef limestone. Sustainability 14, 13761.
Zhang, Y., Luo, H., Chen, P., Liu, E., Chen, Y., 2022b. Mechanical properties and binary-medium-based constitutive model for coral-reef limestone samples subjected to uniaxial loading. Sustainability 14, 12193.

Dr. Qingshan Meng is currently a full professor at Institute of Rock and Soil Mechanics (IRSM), Chinese Academy of Sciences. He obtained his MEng from Wuhan University of Science and Technology in 2000, and PhD from IRSM, Graduate School of Chinese Academy of Sciences in 2003. He has been engaged in researches on engineering geology and mechanical properties of coral reefs. He achieved some results in the knowledge of the morphology and stratigraphic structure of reef islands, the reinforcement technology and effect evaluation of reef sand foundation, the service performance enhancement of seawater-mixed reef sand concrete, and the damage mechanism and engineering utilization of coral reef limestone.